Contents lists available at ScienceDirect

Chemical Engineering Journal

A highly efficient and suitable spectral profile Cr^{3+}-doped garnet near-infrared emitting phosphor for regulating photomorphogenesis of plants

Xikun Zou [a,b], Xiaojun Wang [c], Haoran Zhang [a,b], Yunyan Kang [d], Xian Yang [d], Xuejie Zhang [a,b,*], Maxim S. Molokeev [e], Bingfu Lei [a,b,*]

[a] *Key Laboratory for Biobased Materials and Energy of Ministry of Education, College of Materials and Energy, South China Agricultural University, Guangdong, Guangzhou 510642, China*
[b] *Maoming Branch, Guangdong Laboratory for Lingnan Modern Agriculture, Guangdong, Maoming 525100, China*
[c] *Department of Physics, Georgia Southern University, Statesboro, GA 30460, USA*
[d] *College of Horticulture, South China Agricultural University, Guangzhou 510642, China*
[e] *SB RAS, Kirensky Inst Phys, Lab Crystal Phys, Krasnoyarsk 660036, Russia*

ARTICLE INFO

ABSTRACT

Far-red/phytochrome (P$_{FR}$) plays a key role in photomorphogenesis of plants. However, how to obtain a near-infrared (NIR) emitting phosphor with high external quantum efficiency (EQE), suitable spectral profile, and low thermal quenching remains a huge challenge. Herein, a NIR phosphor, Gd$_{2.4}$Lu$_{0.6}$Ga$_4$AlO$_{12}$:Cr^{3+},H$_3$BO$_3$ (GLGA:Cr^{3+}) was developed via regulating the crystal field environment and adding fluxes, which exhibits a peak maximum at 728 nm with a relatively narrow full-width at half maximum (FWHM) of 107 nm, matching well with the absorption band of P$_{FR}$. Upon 450 nm excitation, the internal quantum efficiency (IQE) and EQE of the optimal phosphor are 90.3% and 32.0%, respectively. At 423 K, the integrated emission intensity of the investigated phosphor is about 75% of that at room temperature. Benefiting from the excellent optical performance, a NIR phosphor-converted light-emitting diode (pc-LED) was fabricated, which shows a NIR output power of 505.99 mW and photoelectric conversion efficiency of 11.24% at 300 mA. Moreover, plant growth experiments demonstrate that the biomass of pea seedlings is increased by 67.72% under supplementary NIR light irradiation. The findings of this research will motivate further research on new Cr^{3+}-doped NIR phosphors for regulating photomorphogenesis of plants.

1. Introduction

Near-infrared (NIR, 650–1400 nm) spectroscopy possesses unique advantages, such as noninvasive, real-time monitoring, and fast analysis, which enable its application in many fields like bioimaging, night vision illumination, and food analysis [1–3]. Phosphor-conversion light-emitting diode (pc-LED) devices combining broadband NIR phosphors with commercially efficient blue LED chips have the merits of broadband emission, small size, high radiant flux, excellent durability. The key broadband NIR phosphors can be obtained by doping Eu^{2+}, Mn^{2+}, Mn^{4+}, and Cr^{3+}. Unfortunately, due to the lack of suitable hosts, only a few Eu^{2+}-doped phosphors have been reported in the literature, for example, Ca$_3$Sc$_2$Si$_3$O$_{12}$:Eu^{2+}, K$_3$LuSi$_2$O$_7$:Eu^{2+}, and Ba$_3$ScB$_3$O$_9$:Eu^{2+}

[4–6]. Additionally, they are characterized by low luminescence intensity and low-efficiency blue light pumped. Mn^{2+}-doped phosphor such as Ca$_3$MgSi$_2$O$_8$:Eu^{2+}, Mn^{2+} shows a NIR emission peaking at 700 nm, but can only be excited with UV light [7]. Most Mn^{4+}-doped materials show relatively short wavelength and weak absorption in blue light region, which suspends their application [8]. Comparatively, Cr^{3+} ion has been considered as an ideal NIR luminescent center, and it is easy to generate broadband emission with ^{4}T$_{2g}$→^{4}A$_{2g}$ transition through regulating the crystal field environment [9–11]. Guided by this design principle, plenty of Cr^{3+}-doped phosphors have been investigated aiming at NIR pc-LED application, such as La$_3$Ga$_5$GeO$_{14}$:Cr^{3+} (FWHM = 330 nm, λ_{em} = 750 nm), K$_2$Ga$_2$Sn$_6$O$_{16}$:Cr^{3+} (FWHM = 220–230 nm, λ_{em} = 830 nm), LiIn$_2$SbO$_6$:Cr^{3+} (FWHM = 225 nm, λ_{em} = 970 nm),

Cs$_2$AgInCl$_6$:Cr^{3+} (FWHM = 180 nm, λ_{em} = 1010 nm), etc. [12–15]. The crucial features of these NIR phosphors for bioimaging and food analysis are the ultra-broadband emission with longer wavelength to achieve deeper penetration depths in tissue. Obviously, the emission spectral profile of these NIR phosphors does not match well with the absorption of far-red/phytochrome (P$_{FR}$) of plants. As known, the signal transmitted with the red/phytochrome (P$_R$) and P$_{FR}$ is one of the factors affecting photomorphogenesis. P$_{FR}$ shows an absorption band peaked at 730 nm with a FWHM of 80 nm, which plays an essential role in seed germination, flowering regulation, leaf and stem expansion. However, Cr^{3+}-doped NIR phosphors targeting the absorption of P$_{FR}$ have rarely been reported.

Cr^{3+} photoluminescence in an octahedral system is determined by relative energies and sequence of the two lowest energy excited states ^2E_g and $^4T_{2g}$. When Cr^{3+} ions occupy strong crystal field sites, the ^2E_g level lies below the $^4T_{2g}$ level and the emission spectrum shows a narrow emission line due to the spin-forbidden $^2E_g \rightarrow ^4A_{2g}$ transition [16]. In contrast, when Cr^{3+} ions occupy weak crystal field sites, the lowest excited state is the $^4T_{2g}$ state and the emission spectrum of $^4T_{2g} \rightarrow ^4A_{2g}$ transition consists of a (weak) zero-phonon line and a Stokes shifted broadband involving phonon sidebands [17]. Naturally, the Cr^{3+} ions occupy intermediate crystal field sites, both narrow ^2E_g and broad $^4T_{2g}$ emission are observed because the two low-lying levels are in thermal equilibrium. Therefore, to obtain an ideal NIR phosphor for plant growth, the host should provide octahedral sites with an intermediate crystal field [18,19]. Garnet phosphors doped with Cr^{3+} exhibit high quantum efficiency (QE) and excellent thermal stability in NIR regions. In the case of strong crystal field like in Y$_3$Al$_5$O$_{12}$:Cr^{3+}, the relatively narrow emission band and emission peak at around 700 nm originate from the $^2E_g \rightarrow ^4A_{2g}$ transition [20]. Substituting Al^{3+} with Ga^{3+} ions leads to a weaking of the crystal field, and in this case the emission gives a broad band peaking at around 720 nm due to the $^4T_{2g} \rightarrow ^4A_{2g}$ transition [21]. Therefore, gallium garnets are more suitable for satisfying the photomorphogenesis needs of plants. Gd$_3$Ga$_5$O$_{12}$:Cr^{3+} has a typical garnet structure, which can be excited by blue light and exhibits an emission band in the range of 630–850 nm with the emission peak at 717 nm [21]. Unfortunately, the reported low internal/external quantum efficiency (IQE/EQE) and unsuitable spectrum profile limited its application in plant cultivation. Cationic substitution is one of the effective strategies to regulate crystal field strength and improve luminescence performances. For example, Liu et al. [22] obtained controllable Cr^{3+} emission tuning from 965 to 892 nm in LiIn$_2$SbO$_6$ through chemical unit cosubstitution of [Zn^{2+}–Zn^{2+}] for [Li$^+$–In^{3+}]. Basore et al. [23] reported the IQE of Cr^{3+} emission can be significantly improved to nearly 100% via the substitution of ScO$_6$ with smaller AlO$_6$ octahedrons to inhibit the formation of antisite defects.

Inspired by these regulating strategies, by introducing the smaller Lu^{3+} and Al^{3+} into Gd$_3$Ga$_5$O$_{12}$:Cr^{3+} and adding fluxes, a new NIR phosphor Gd$_{2.4}$Lu$_{0.6}$Ga$_4$AlO$_{12}$:Cr^{3+},H$_3$BO$_3$ (GLGA:Cr^{3+}) with intermediate crystal field was obtained, which gives an emission at 728 nm with a FWHM of 107 nm and well matches the absorption band of P$_{FR}$. Thanks to the excellent EQE and low thermal quenching behavior, a NIR pc-LED was fabricated by integrating the optimal sample on chip-on-board (COB) blue LED, which has a high output power of 505.99 mW and photoelectric efficiency of 11.24% at 300 mA. Furthermore, the NIR pc-LEDs were applied to plant light sources and its ability to enhance biomass was evaluated in pea seedlings.

2. Experimental

2.1. Materials and synthesis

Gd$_3$Ga$_{4.87-x}$Al$_x$O$_{12}$:0.13Cr^{3+} ($0 \leq x \leq 3$), Gd$_{3-y}$Lu$_y$Ga$_{4.87}$O$_{12}$:0.13Cr^{3+} ($0 \leq y \leq 0.9$), Gd$_{2.4}$Lu$_{0.6}$Ga$_{4-x}$AlO$_{12}$:xCr^{3+} ($0 \leq x \leq 0.21$), and Gd$_{2.4}$Lu$_{0.6}$Ga$_{3.87}$AlO$_{12}$:0.13Cr^{3+}, y wt%H$_3$BO$_3$ ($0 \leq y \leq 5$) phosphors were synthesized via the traditional high-temperature solid-state reaction. Lu$_2$O$_3$ (Shanghai Sheeny Metal Material, 99.99%), Gd$_2$O$_3$ (Macklin, 99.99%), Ga$_2$O$_3$ (Macklin, 99.8%), Al$_2$O$_3$ (Macklin, 99.99%), Cr$_2$O$_3$ (Aladdin, 99.9%) and H$_3$BO$_3$ (Macklin, 99.9%) were used as raw materials. The raw materials were weighed stoichiometrically, mixed and grounded in an agate mortar for 20 min, then transferred to a corundum crucible. Finally, its mixture was heated to 1350 °C at 5 °C/min in a muffle furnace and maintained for 5 h. After the annealing process, the obtained material was naturally cooled to room temperature and was ground into powder for further characterization steps. The NIR pc-LED was fabricated by using the optimal sample and the COB blue LED (λ_{em} = 450 nm, 5 W). The mass ratio of the epoxy resin to phosphor was fixed at 1:3.5.

2.2. Plant cultivation

The pea seedling (*Pisum sativum* L.) cultivation experiments consist of a control group (represented as CK) and an experimental group (represented as NIR-P). Specifically, the CK was illuminated with commercial red- and blue- LEDs; the light sources of NIR-P were composed of commercial red-, blue- LEDs, and the fabricated NIR pc-LEDs, which the intensity ratio from 618 nm to 728 nm reaches about 2:1 (Fig. S1). Afterward, the uniform pea seedlings are randomly arranged in CK and NIR-P. There were four replications for each treatment and five seedlings for each replication. The pea seedlings were illuminated with a light intensity of 95–105 μmol·m^{-2}·s^{-1} for 24 h.

2.3. Characterization and measurements

The X-ray diffraction (XRD) patterns were taken with a D8 Advance X-ray diffractometer with 40 kV operating voltage and 15 mA current settings. Rietveld refinements were performed using TOPAS 4.2. The sample powder morphology was observed using a Sirion-400 field emission scanning electron microscope (FE-SEM). Electron paramagnetic resonance (EPR) spectroscopy were measured by Bruker A300. X-ray photoelectron spectrometer (XPS) were recorded on a Thermo Scientific Escalab 250Xi. The fluorescence photographs of phosphor particles were obtained by Nikon Eclipse Ti2 inverted fluorescence microscope. The photoluminescence (PL), photoluminescence excitation (PLE) and temperature-dependent emission spectra were performed on an Edinburgh FLS920 fluorescence spectrophotometer. The QE was performed by a Quantaurus-QY Plus C13534-12. Diffuse reflection spectra (DRS) were measured by a Shimadzu UV-3600 plus. Temperature-dependent decay curves were recorded by an Edinburgh FLS1000 fluorescence spectrophotometer. Electroluminescence, output power, and photoelectric efficiency of the NIR pc-LED were achieved by a HP8000 photoelectric measuring system.

3. Results and discussion

3.1. Regulation of spectral profile

In order to obtain the spectral profile of Gd$_3$Ga$_5$O$_{12}$:Cr^{3+} more suitable for the absorption band of P$_{FR}$, the luminescence properties of the phosphor could be tuned and improved via modifying the composition of matrix. Firstly, we introduced smaller Al^{3+} to substitute Ga^{3+} sites in Gd$_3$Ga$_5$O$_{12}$:Cr^{3+} compound to realize the blue-shift of the emission band. With increasing Al^{3+} content, the emission peak of Gd$_3$Ga$_{4.87-x}$Al$_x$O$_{12}$:0.13Cr^{3+} (the dopant concentration of Cr^{3+} is selected from the optimal sample.) changes from 746 to 714 nm, attributed to the relatively strong crystal field induced by the shrinkage of the crystal lattice (Fig. 1a). Unfortunately, the PL intensity decreases with increasing Al^{3+} concentration, which may be partly caused by the presence of relatively strong $^2E_g \rightarrow ^4A_{2g}$ line (known as R-line) emission superimposed on the $^4T_{2g} \rightarrow ^4A_{2g}$ emission band (Fig. S2). Generally, incorporation of Lu^{3+} in Gd$_3$Al$_5$O$_{12}$ can form (Gd,Lu)$_3$Al$_5$O$_{12}$ solid solutions, which decreases lattice parameters and increases optical
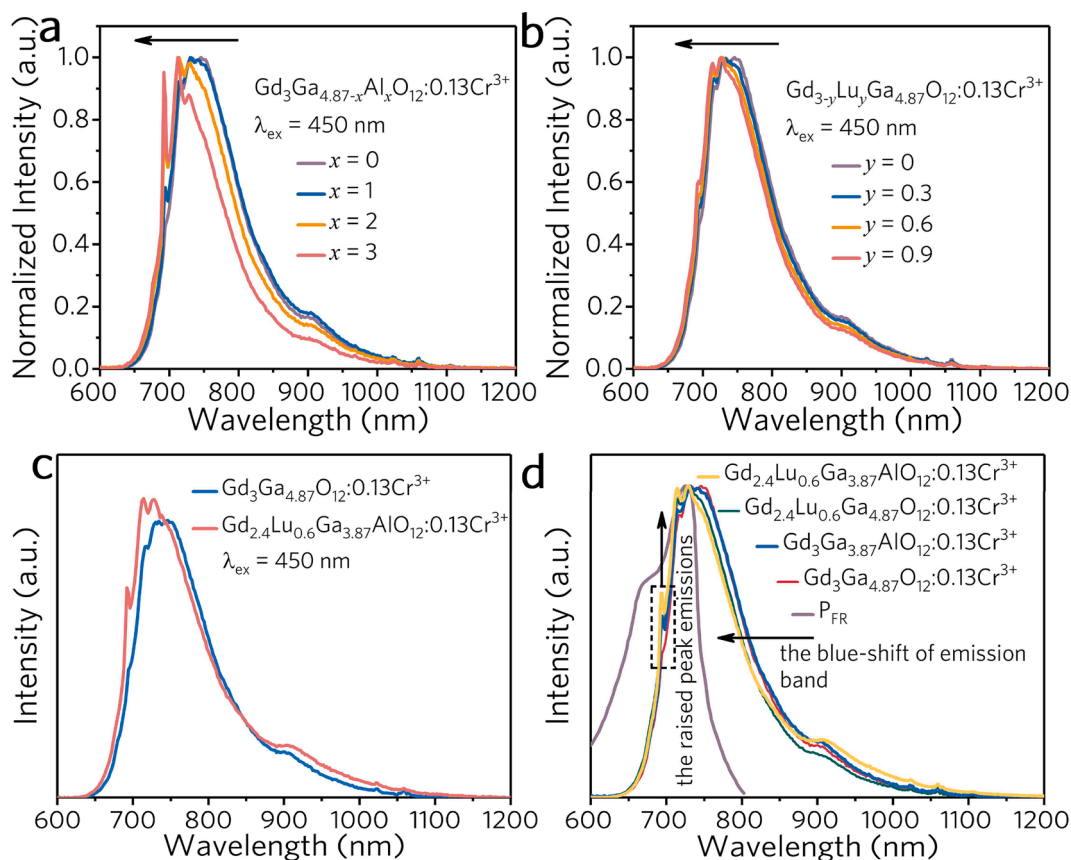
Fig. 1. The normalized emission spectra of (a) $Gd_3Ga_{4.87-x}Al_xO_{12}:0.13Cr^{3+}$ and (b) $Gd_{3-y}Lu_yGa_{4.87}O_{12}:0.13Cr^{3+}$; (c) The PL spectra of $Gd_3Ga_{4.87}O_{12}:0.13Cr^{3+}$ and $Gd_{2.4}Lu_{0.6}Ga_{3.87}AlO_{12}:0.13Cr^{3+}$; (d) The comparisons between the normalized PL spectra of different phosphors ($Gd_{2.4}Lu_{0.6}Ga_{3.87}AlO_{12}:0.13Cr^{3+}$, $Gd_{2.4}Lu_{0.6}Ga_{4.87}O_{12}:0.13Cr^{3+}$, $Gd_3Ga_{3.87}AlO_{12}:0.13Cr^{3+}$, and $Gd_3Ga_{4.87}O_{12}:0.13Cr^{3+}$) and the absorption spectrum of P_{FR}.

bandgaps [24]. Based on this, we also introduced smaller Lu^{3+} to substitute Gd^{3+} sites in $Gd_3Ga_5O_{12}:Cr^{3+}$ compound to regulate the spectral profile and lower the thermal quenching. The substitution of Lu^{3+} for Gd^{3+} located in the second coordination sphere causes the size shrinkage of the dodecahedron, thereby leading to the increase of crystal field splitting. As expected, with tinily increasing Lu^{3+} concentration, the emission spectra exhibit slight blue-shift (Fig. 1b). The luminescence intensity of Cr^{3+} ions initially increases with growing amount of Lu^{3+} ions in the matrix and reaches the maximum at y = 0.06 (Fig. S3). Considering the emission spectrum profile and emission intensity comprehensively, the optimal substitute contents of Al^{3+} and Lu^{3+} in $Gd_{3-y}Ga_{4.87-x}O_{12}:0.13Cr^{3+}$ are x = 1.0 and y = 0.6, respectively. The

$Gd_{2.4}Lu_{0.6}Ga_{3.87}AlO_{12}:0.13Cr^{3+}$ sample not only has higher luminescence intensity than that of $Gd_3Ga_{4.87}O_{12}:0.13Cr^{3+}$ but also exhibits greater spectral overlap with the absorption of P_{FR} (Fig. 1c). The enhanced spectral overlap originates from the raised peak emissions and the blue-shift of emission band (Fig. 1d), which provides a better spectral matching for the needs of photomorphogenesis in plants.

3.2. Phase purity and structure analysis

The luminescence performance of phosphors is strongly dependent on crystallinity [25,26]. To enhance the luminescence of GLGA:$0.13Cr^{3+}$, the flux of H_3BO_3 was added. Fig. 2a shows the X-ray

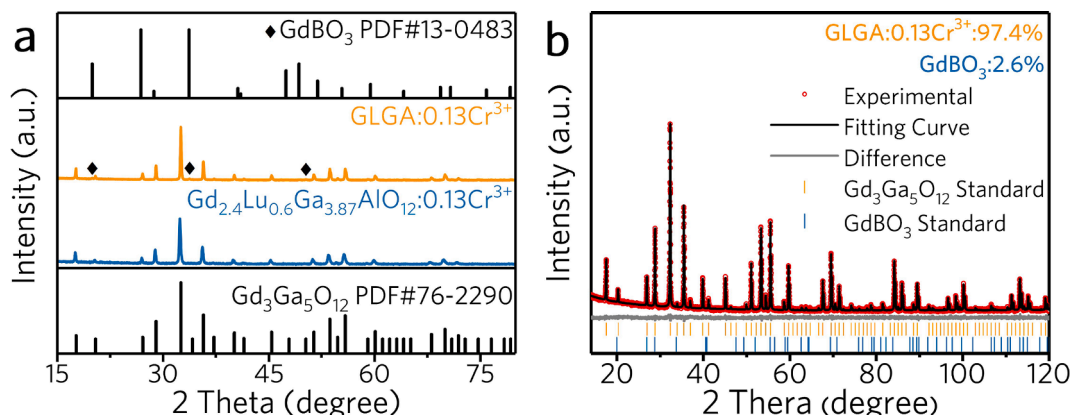**Fig. 2.** (a) XRD patterns of GLGA:$0.13Cr^{3+}$ and GLGA:$0.13Cr^{3+}$ (b) Rietveld refinement XRD pattern of GLGA:$0.13Cr^{3+}$ sample.

powder diffraction (XRD) patterns of flux-free and flux-adding samples. It can be clearly seen that the diffraction peaks of the flux-free sample match well with the reference pattern of the $Gd_3Ga_5O_{12}$ phase (PDF #76-2290) without any impurity. The XRD pattern of H_3BO_3-adding sample can be also well indexed to $Gd_3Ga_5O_{12}$ standard data except for several impurity peaks of $GdBO_3$ (PDF#13-0483). Notably, the diffraction peaks of GLGA:0.13Cr^{3+} is much higher and narrower than those of flux-free sample under the same measurement conditions (Fig. S4), confirming the crystallinity of the phosphor is obviously enhanced. To obtain detailed crystal structure information and the impurity content, a Rietveld refinement of the GLGA:0.13Cr^{3+} samples was carried out by using the crystallographic data of $Gd_3Ga_5O_{12}$ as a starting mode and the corresponding results are shown in Fig. 2b and list in Table S1-S3. The refinement result shows that the diffraction peaks are composed of 97.4% main phase and 2.6% secondary phase. The low residual factors of $\chi^2 = 1.26$, $R_{wp} = 2.70$, and $R_p = 2.13$ mean that the refinement result is satisfactory. $Gd_3Ga_5O_{12}$ has a cubic structure with a space group of *Ia-3d* [27]. In $Gd_3Ga_5O_{12}$ model, where Gd^{3+} sites were replaced by Gd^{3+}/Lu^{3+}, $[GaO_4]$ (Ga1 site) tetrahedrons and $[GaO_6]$ (Ga2 site) octahedrons were occupied by $Ga^{3+}/Cr^{3+}/Al^{3+}$ (Fig. S5). Considering the same valence state and similar ionic radii of Ga^{3+} (0.62 Å) and Cr^{3+} (0.62 Å) at 6-coordinated octahedral, $[GaO_6]$ (Ga2) octahedral sites are considered as ideal crystallographic position for the incorporation of Cr^{3+} activators. The preferred occupations of Cr^{3+} in Ga2 sites and Al^{3+} in Ga1 sites are observed in Rietveld refinement as expected. The smaller ion radii of Lu^{3+} (1.02 Å, CN = 8) and Al^{3+} (0.39 Å, CN = 4) than that of Gd^{3+} (1.05 Å, CN = 8) and Ga^{3+} (0.47 Å, CN = 4) result in the lattice constant decreasing from 12.3782 Å ($Gd_3Ga_{4.87}O_{12}$:0.13Cr^{3+}) to 12.3098 Å (GLGA:0.13Cr^{3+}). The enhanced crystal field strength by introducing Lu^{3+} and Al^{3+} can explain the reason for the blue-shift of emission (Table S3). The impurity $GdBO_3$ has no suitable cation sites for Cr^{3+} due to the large difference in ionic radii, which exhibits no influence on PL properties of GLGA:0.13Cr^{3+}.

The as-synthesized GLGA:0.13Cr^{3+} phosphor presents irregular morphology and an average particle size of about 30 μm (Fig. S6). The larger size of the phosphor indicates that the synthesized phosphor has high crystallinity, which is important to obtain high QE. These microparticles of GLGA:0.13Cr^{3+} were further verified by fluorescence microscope photographs, which give uniform luminescence under 465 nm excitation (Fig. 3a). The elemental mapping results show that the Lu, Gd, Ga, Al, Cr, O and B elements are uniformly presented in the phosphor particle, which confirm that the Cr^{3+} is successfully doped (Fig. 3b). Cr^{3+} is a highly efficient luminescent activator, while the Cr^{4+} often

coexists with Cr^{3+}-doped NIR phosphors during the synthesis [25]. EPR and XPS are effective methods to analyze the valence state of ions. According to the theory of Landry, the isolated Cr^{3+} ions and the Cr^{3+}-Cr^{3+} exchange coupled pairs are assigned to the low field portion and the high field portion, respectively [28]. At room temperature, the EPR signals of the GLGA:0.13Cr^{3+} are observed at g = 4.22 and g = 1.97, the former is derived from isolated Cr^{3+} and the latter is attributed to the first nearest-neighbor Cr^{3+} ion pairs (Fig. 3c) [17,29,30]. The XPS spectrum of GLGA:0.13Cr^{3+} also confirms the presence of Lu, Gd, Ga, Al, Cr and B in the sample (Fig. S7), which is consistent with the results of elemental mapping. Two peaks at 576.4 eV and 580.9 eV can be observed in enlarged XPS, which are belong to the Cr 2p3/2 core-level electrons of Cr^{3+} (Fig. 3d) [31]. These results further confirm that Cr^{4+} is not present in GLGA:Cr^{3+}, although the investigated phosphor was prepared in air.

3.3. Optical properties

Compared with the undoped GLGA, the strong absorption bands of GLGA:0.13Cr^{3+} are distributed in the ultraviolet, blue, and red regions, which are ascribed to $^4A_{2g} \rightarrow ^4T_{1g}(P)$, $^4A_{2g} \rightarrow ^4T_{1g}(F)$, and $^4A_{2g} \rightarrow ^4T_{2g}(F)$ transitions of Cr^{3+}, respectively (Fig. 4a). No Cr^{4+} typical absorption band in the 800–1400 nm range is observed, which is consistent with the EPR and XPS results. The band gap is estimated to be 4.34 eV from the calculated Kubelka−Munk absorption spectrum of the undoped GLGA sample (inset of Fig. 4a). Excitation and emission spectra of GLGA:0.13Cr^{3+} are depicted in Fig. 4b. The excitation bands are well consistent with these in DRS. Under 446 nm excitation, GLGA:0.13Cr^{3+} shows a broad NIR emission peaking at 728 nm with a FWHM value of 107 nm, arising from the $^4T_{2g}(F)$ to $^4A_{2g}$ transition of Cr^{3+}. Some sharp lines peaking at 696 nm, 714 nm, and 728 nm are also observed on the shorter wavelength edge of the broad band emission. The presence of sharp lines and the narrow bandwidth for the Cr^{3+} emission in GLGA is partly caused by the presence of relatively strong $^2E_g \rightarrow ^4A_{2g}$ line (also known as R-line) emission superimposed on the $^4T_{2g} \rightarrow ^4A_{2g}$ emission band. To clarify the energy level of Cr^{3+}, the Tanabe-Sugano diagram is shown in Fig. 4c. The corresponding crystal field parameters (*Dq* and *B*) are calculated by the following equations [32]:

$$D_q = \frac{Ea^4T_{2g}}{10} \qquad \qquad 3\text{-}1$$

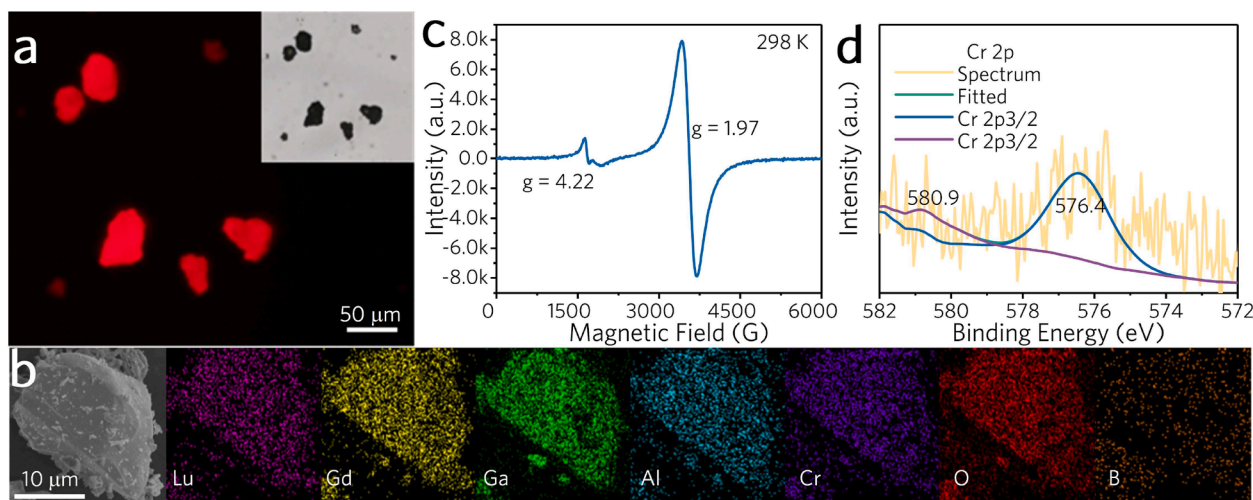$$B = D_q \frac{x^2 - 10x}{15(x - 8)} \qquad \qquad 3\text{-}2$$

Fig. 3. (a) Fluorescence microscope photographs of the GLGA:0.13Cr^{3+} particles with and without 465 nm excitation; (b) Element mapping images of Lu, Gd, Ga, Al, Cr, O, B for the selected GLGA:0.13Cr^{3+} particle; (c) EPR spectrum of GLGA:0.13Cr^{3+} at 298 K. (d) XPS spectra of GLGA:0.13Cr^{3+} in Cr 2p levels.
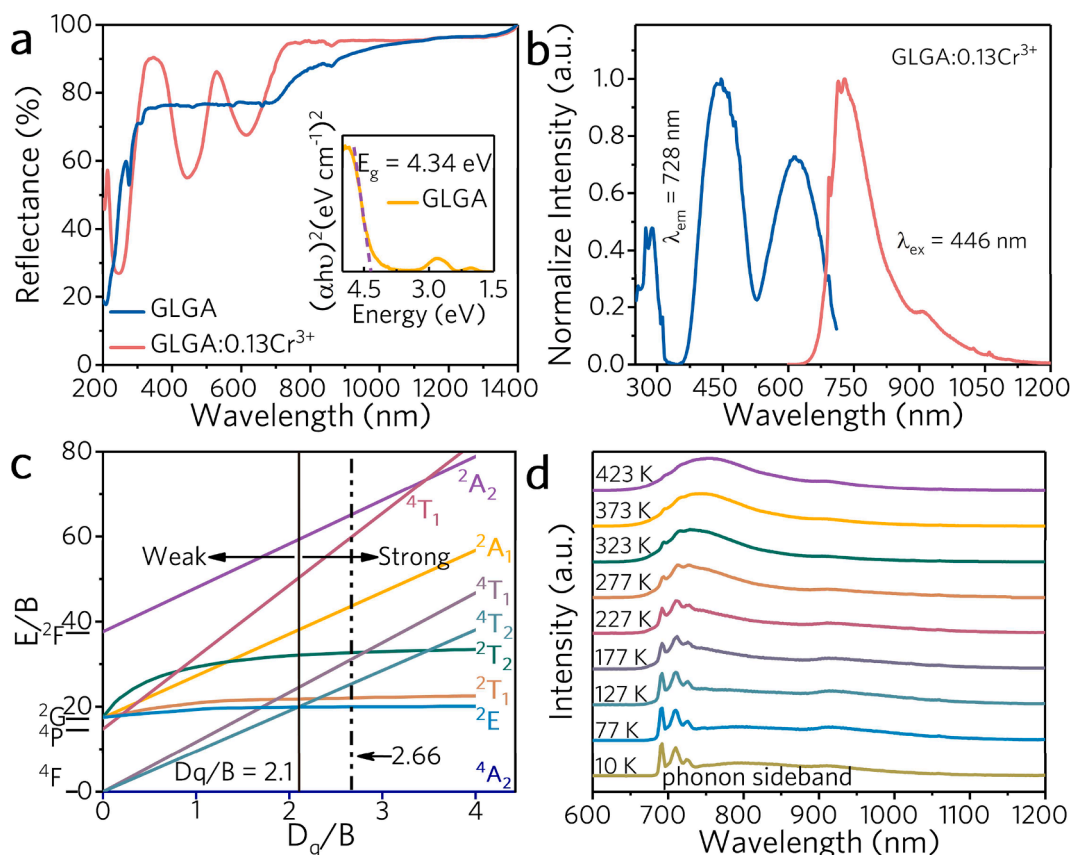
Fig. 4. (a) DRS of undoped GLGA and GLGA:0.13Cr^{3+}; (b) PLE and PL spectra of GLGA:0.13Cr^{3+}; (c) Tanabe–Sugano energy level diagram of Cr^{3+} in an octahedral crystal field; (d) Temperature-dependent PL spectra of the GLGA:0.13Cr^{3+} under 450 nm excitation.

$$x = \frac{Ea^4T_{1g} - Ea^4T_{2g}}{D_q} \qquad 3\text{-}3$$

where D_q is the crystal field parameter, B represents the Racah parameter, Ea^4T_{1g} and Ea^4T_{2g} are the $^4T_{1g}$ and $^4T_{2g}$ levels, respectively. Accordingly, in the GLGA:0.13Cr^{3+}, D_q, B and D_q/B values were calculated to be 1623 cm^{-1}, 610 cm^{-1} and 2.66, respectively. The result shows that the introduction of Lu^{3+} and Al^{3+} ions can significantly increase the crystal field strength (seen in Table 1). Moreover, by comparison of the crystal field parameters and FWHM between GLGA:0.13Cr^{3+} and other Cr^{3+}-activated NIR phosphors, it can be found that the FWHM of Cr^{3+} emission can be effectively regulated through controlling the crystal field strength. It should be noted, however, that when determining the energy levels of $^4T_{2g}$ and $^4T_{1g}$, their strong phonon coupling has to be taken into account. It is evident that their equilibrium energy levels are not given simply by the peak energy values of the PLE bands, but by the energy of the electronic zero-phonon line (ZPL) energies [33]. However, for simplicity, we used the former values

Table 1
FWHM and crystal field parameters of different Cr^{3+}-doped NIR phosphors.

Phosphor	FWHM	D_q (cm^{-1})	B (cm^{-1})	D_q/B	Ref.
Y$_{1.5}$Ca$_{1.5}$Al$_{3.5}$Si$_{1.5}$O$_{12}$: Cr^{3+}	~166	1639	390	2.38	[11]
MgTa$_2$O$_6$:Cr^{3+}	140	1471	588	2.50	[32]
LiInSi$_2$O$_6$:Cr^{3+}	143	~1342	767	1.75	[35]
La$_2$MgZrO$_6$:Cr^{3+}	210	1542	619	2.49	[36]
ScBO$_3$:Cr^{3+}	~120	1400	651	2.15	[37]
Gd$_3$Ga$_5$O$_{12}$:Cr^{3+}	–	1597	626	2.55	[21]
GLGA:0.13Cr^{3+}	107	1623	610	2.66	This work

for equations (3–1)−(3–3) (see details in Ref. [34]).

PL spectra of GLGA:xCr^{3+} ($0.01 \leq x \leq 0.21$, step of 0.02) with variable Cr^{3+} concentrations are shown in Fig. S8a. With increasing the dopant concentration of Cr^{3+}, the maximum intensity is observed at $x = 0.13$. Remarkably, when the Cr^{3+} dopant concentration is increased from 0.01 to 0.13, the maximum emission peak shifts from 714 nm to 728 nm. Generally, the spectral red-shift of Cr^{3+}-doped phosphors is attributed to the decrease of crystal field strength and reabsorption [38]. It is believed that the red-shift is not attributed to the lattice shrinkage associated with the increase of the doping concentration because the ionic radii of Cr^{3+} are similar to that of Ga^{3+}. Due to the existing overlap between the emission and absorption in 620–740 nm region, the blue wing intensity of the emission band decreases with increasing the dopant concentration of Cr^{3+}, and the emission shows a slight red-shift (Fig. S8b and c). Thus, the reabsorption between activators becomes the dominating reason for the red-shift. To enhance the luminescence by improving the crystallinity, flux of H$_3$BO$_3$ was added during the synthesis. It is noted that the emission intensity of GLGA:0.13Cr^{3+} is greatly enhanced by 2 times compared with the flux-free sample (Fig. S9). Meanwhile, the optimal sample of GLGA:0.13Cr^{3+} has the IQE/EQE values of 90.3/32.0% (Fig. S10), better than most Cr^{3+}-doped NIR phosphors previously reported (see Table 2).

To gain further insight in the luminescence properties of Cr^{3+} in the GLGA, low temperature measurements were done (Fig. 4d). GLGA:0.13Cr^{3+} shows both narrow and broad band emission at room temperature, which indicates that Cr^{3+} is at intermediate crystal field sites [9,10]. In such a system, the energy difference between two excited states ^2E_g and $^4T_{2g}$ is small. PL spectrum at 10 K is composed of ZPL and some weak vibronic sidebands on the low-energy side of this line. A thermal equilibrium between the doublet and quartet levels occurs with raising the temperature. Accordingly, both ^2E_g line emission and $^4T_{2g}$

Table 2
Optical properties of different Cr^{3+}-doped NIR phosphors and NIR pc-LED device parameters.

Phosphors	IQE (%)	EQE (%)	Thermal stability (%) @temperture	Input electricalpower (mW)	NIR output power (mW)@photoelectric efficiency	Ref.
$Ga_{1.6}Sc_{0.4}O_3$:Cr^{3+}	99	–	–	–	66.09mW@–	[17]
$Ca_2LuHf_2Al_3O_{12}$:Cr^{3+}	–	–	~65@423 K	292.6	46.09@15.75%	[1]
$LiInSi_2O_6$:Cr^{3+}	~75	–	~77%@423 K	289.8	51.6@17.8%	[35]
$Ca_3Sc_2Si_3O_{12}$:Cr^{3+}	92.3	21.5	97.4%@423 K	2892	109.9@~3.8%	[30]
K_2NaScF_6:Cr^{3+}	74	–	89.6@423 K	1094	159.72@14.6%	[43]
				4499	393.73@8.75	
$Gd_3Sc_2Ga_3O_{12}$:Cr^{3+}	91	–	92@423 K	750	~105@14%	[23]
				4541	~470@10.35%	
				9750	750.8@7.7%	
$ScBO_3$:Cr^{3+}	65	–	51@423 K	371	26@7%	[37]
$LiScP_2O_7$:Cr^{3+},Yb^{3+}	74	39	79@373 K	300	36@12%	[44]
$Ca_2LuZr_2Al_3O_{12}$:Cr^{3+}, Yb^{3+}	77.2	–	69.1@423 K	292.3	41.8@14.3%	[45]
GLGA:$0.13Cr^{3+}$	90.3	32.0	75@423 K	1086.40	162.26@14.89%	This work
				4500.00	505.99@11.24%	

band emission are observed (Fig. 4d). Meanwhile, the broadening of emission band becomes remarkable due to the overlap of broad band ($^4T_{2g} \rightarrow ^4A_{2g}$) and ZPL/phonon sidebands ($^2E_g \rightarrow ^4A_{2g}$). Luminescence thermal stability of NIR phosphor is a key parameter for pc-LEDs. Therefore, it is necessary to evaluate the luminescence thermal quenching behavior of the GLGA:$0.13Cr^{3+}$ NIR phosphor. For the present work, the focus is on the high temperature regime from 298 to 423 K. The integrated PL intensity of GLGA:$0.13Cr^{3+}$ decreases with increasing temperature (Fig. 5a). At 423 K (Fig. 5b), the integrated emission intensity of GLGA:$0.13Cr^{3+}$ is about 75% of that at room temperature (Table 2). It is noted that the FWHM increases from 1940 cm^{-1} to 2350 cm^{-1} when the temperature rises from 298 to 423 K (Fig. 4d and 5a), attributed to the electron–phonon interaction.

Moreover, the values of Stokes shift and Huang-Rhys parameter S can be evaluated at a low temperature. As shown in Fig. S11, the Stokes shift is 1836 cm^{-1} at 10 K, and the energy difference between the ZPL and its phonon sidebands is one of the vibrational modes ($\hbar w$) that couple with the $^4T_{2g}(F) \rightarrow ^4A_{2g}$ transition, calculated to be ~366 cm^{-1} [30,39]. According to $(2S + 1)\hbar w$, the S is obtained to be between 2 and 3, which is smaller than that of Sc_2O_3:Cr^{3+} ($S = 4.32$), Cs_2NaAlF_6:Cr^{3+} ($S = 4.5$), $YAl_3(BO_3)_4$:Cr^{3+} ($S = 5.93$) and $GdAl_3(BO_3)_4$:Cr^{3+} ($S = 5.37$) [40–42]. As known, a stronger electron–phonon coupling not only causes broader FWHM of Cr^{3+} emission but also results in higher thermal quenching. The activation energy (E_a) can further evaluate thermal stability, which can be calculated by the following formula:
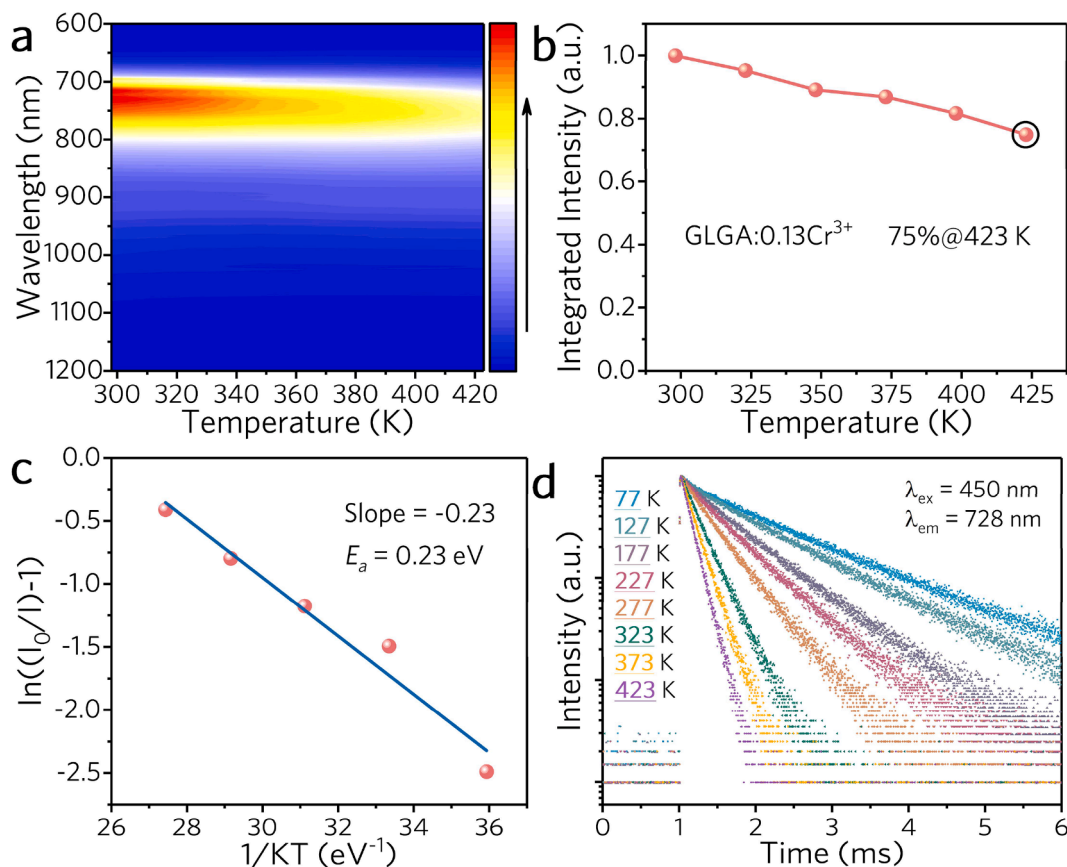

Fig. 5. (a) Temperature-dependent emission spectra of GLGA:$0.13Cr^{3+}$; (b) Temperature-dependent normalize integrated intensities; (c) The function of $1/KT$ and ln $((I_0/I)-1)$; (d) The temperature-dependent decay curves of GLGA:$0.13Cr^{3+}$ monitored at 728 nm upon excitation of 450 nm.
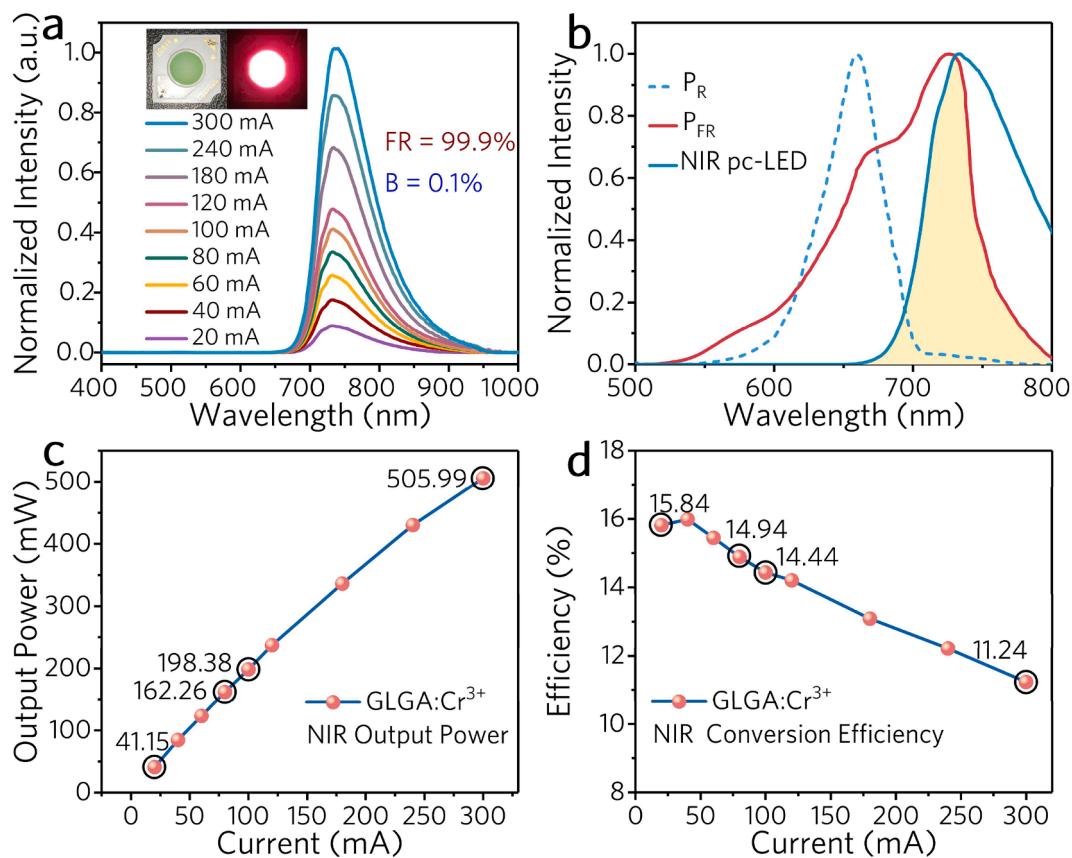
Fig. 6. (a) The emission spectra of the fabricated NIR pc-LED depending on the driving current, and the inset is photographs (power off and power on) of the NIR pc-LED device; (b) The fabricated NIR pc-LED emission spectrum and absorption curves of P_R and P_{FR}; (c) NIR output power and (d) photoelectric conversion efficiency under different driving currents.

$$I_T = \frac{I_0}{1 + c*exp\left(-\frac{Ea}{KT}\right)} \qquad \text{3-4}$$

where I_0 is the initial emission intensity and I_T is the emission intensity at temperature T, K is the Boltzmann constant (8.617×10^{-5} eV K^{-1}), c is a constant, and E_a is the activation energy. Fig. 5c shows the slope by fitting $1/KT$ versus $\ln((I_0/I)-1)$ and the activation energy is calculated as 0.23 eV. The results of activation energy and Huang-Rhys parameter S further indicate that GLGA:0.13Cr^{3+} has robust thermal stability, making it a prime candidate for highly efficient NIR pc-LEDs. As shown in Fig. 5d, the temperature-dependent lifetimes decrease significantly

when the temperature increases from 77 K to 423 K because the probability of non-radiative transition increases at elevated temperature. Single-exponential decay curves also demonstrate that impurity GdBO$_3$ has little effect on the GLGA:0.13Cr^{3+} spectra and Cr^{3+} ions only substitute the Ga^{3+} octahedral sites.

3.4. NIR-LED device and application

For demonstration, a high-power NIR pc-LED was fabricated by coating GLGA:0.13Cr^{3+} on a commercial 450 nm COB blue LED (5 W). The fabricated NIR pc-LED exhibits deep-red emission at driving current (Fig. 6a). As the increase of driving currents from 20 mA to 300 mA, all
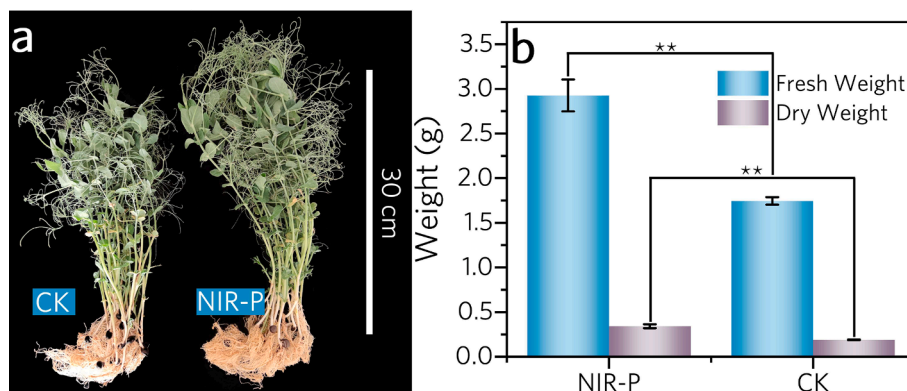

Fig. 7. (a) Morphological characteristics of CK and NIR-P groups after 14 days treatment; (b) Fresh and dry weight in two treatments; N = 6. Average ± standard error (SE). Asterisks indicate significant differences at $p < 0.05$ (*), $p < 0.01$ (**), $p < 0.001$ (***).

spectra show only a NIR emission band without a blue emission band from blue LED, which indicates the title phosphor has a high absorption efficiency for blue light. Unsurprisingly, the emission peak and FWHM of the fabricated NIR pc-LED device can be well matching the absorption band of P_{FR}, indicating that the P_{FR} can be selectively activated rather than P_R (Fig. 6b). As shown in Fig. 6c and d, the NIR output power of NIR pc-LED increases from 41.15 mW@20 mA to 505.99 mW@300 mA, and the photoelectric conversion efficiency of the NIR pc-LED is 14.89% @80 mA and 11.24%@300 mA (see details in Table S4). The NIR output power and photoelectric efficiency of the NIR pc-LED device are superior to the photoelectric performance of most previously reported Cr^{3+}-doped NIR phosphors (Table 2).

To further evaluate the potential of the device for plant growth, pea seedlings (*Pisum sativum* L.) as the model was investigated. After 14 days of pea seedlings growth, morphological photographs, fresh and dry weight of pea seedlings were evaluated and shown in Fig. 7a and b. The CK and NIR-P groups have significant morphological differences, mainly reflected in plant height and the leaf area (Fig. S12). It is noted that the difference is achieved the 79.84% and 67.72% in dry and fresh weight. The increase of biomass is attributed to the increase of internode number rather than the diameter (Fig. S13). In physiological indexes, chlorophyll content is significantly decreased than that in the CK group (Fig. S14), attributed to the fact that the phytochrome-interacting proteins can negatively regulate chlorophyll synthesis in the dark [46]. Therefore, the experiment verifies the promoting the effect of NIR light on the plant stems and leaves growth, which provides a research idea for regulating photomorphogenesis.

4. Conclusions

In conclusion, we have successfully prepared a novel phosphor GLGA:Cr^{3+} through modifying the composition of host crystals, which exhibits relative narrow (FWHM = 107 nm) infrared emission with a maximum at 728 nm that is assigned to the combination of narrow $^2E_g{\rightarrow}^4A_{2g}$ transition and broad band $^4T_{2g}{\rightarrow}^4A_{2g}$ transition, characteristic for Cr^{3+} ions located in an intermediate crystal field environment. The suitable spectral profile of the investigated phosphor can be well fitted with the absorption band of P_{FR}. By adding flux of H_3BO_3, the optimal phosphor exhibits a high crystallinity and larger particle size. Thus, the optimal phosphor exhibits extremely high IQE/EQE values up to 90.3/32.0%, which are superior to most other NIR phosphors. Temperature dependent studies reveal the emission intensity at 423 K can keep 75% of that at room temperature. Benefiting from the excellent optical performance of the title phosphor, a NIR pc-LED was fabricated upon 450 nm COB LED, which exhibits high photoelectric conversion efficiency of 11.24%@300 mA. The experimental results of pea seedlings demonstrated that the biomass was significantly increased by supplementary NIR light irradiation of 700–800 nm. This study provides a reference to regulate the spectral profile of Cr^{3+}-doped NIR phosphors and sheds light on the practical application of Cr^{3+}-doped NIR phosphors in the field of plant lighting.

Declaration of Competing Interest

The authors declare that they have no known competing financial interests or personal relationships that could have appeared to influence the work reported in this paper.

Acknowledgements

Appendix A. Supplementary data

Supplementary data to this article can be found online at https://doi.org/10.1016/j.cej.2021.132003.

References

[1] L.L. Zhang, D.D. Wang, Z.D. Hao, X. Zhang, G.H. Pan, H.J. Wu, J.H. Zhang, Cr^{3+}-doped broadband NIR garnet phosphor with enhanced luminescence and its application in NIR spectroscopy, Adv. Opt. Mater. 7 (2019) 1900185.

[2] R. Li, Y. Liu, C. Yuan, G. Leniec, L. Miao, P. Sun, Z. Liu, Z. Luo, R. Dong, J. Jiang, Thermally stable $CaLu_2Mg_2Si_3O_{12}$:Cr^{3+} phosphors for NIR LEDs, Adv. Opt. Mater. 9 (16) (2021) 2100388.

[3] C.P. Wang, X.M. Wang, Y. Zhou, S. Zhang, C. Li, D.F. Hu, L. Xu, H. Jiao, An ultra-broadband near-infrared Cr^{3+}-activated gallogermanate $Mg_3Ga_2GeO_8$ phosphor as light sources for food analysis, ACS Appl. Electron. Mater. 1 (2019) 1046–1053.

[4] I.V. Berezovskaya, V.P. Dotsenko, A.S. Voloshinovskii, S.S. Smola, Near infrared emission of Eu^{2+} ions in $Ca_3Sc_2Si_3O_{12}$, Chem. Phys. Lett. 585 (2013) 11–14.

[5] J.W. Qiao, G.J. Zhou, Y.Y. Zhou, Q.Y. Zhang, Z.G. Xia, Divalent europium-doped near-infrared-emitting phosphor for light-emitting diodes, Nat. Commun. 10 (2019) 5267.

[6] Z.B. Tang, Q. Zhang, Y.X. Cao, Y.X. Li, Y.H. Wang, Eu^{2+}-doped ultra-broadband VIS-NIR emitting phosphor, Chem. Eng. J. 388 (2020), 124231.

[7] L. Ma, D.-J. Wang, Z.-Y. Mao, Q.-F. Lu, Z.-H. Yuan, Investigation of Eu–Mn energy transfer in $A_3MgSi_2O_8$:Eu^{2+}, Mn^{2+} (A=Ca, Sr, Ba) for light-emitting diodes for plant cultivation, Appl. Phys. Lett. 93 (14) (2008) 144101.

[8] S. Adachi, Review—Mn^{4+}-Activated Red and Deep Red-Emitting Phosphors, ECS J. Solid State Sci. Technol. 9 (1) (2020) 016001.

[9] S. Adachi, Review—Photoluminescence properties of Cr^{3+}-activated oxide phosphors, ECS J. Solid State Sci. Technol. 10 (2) (2021) 026001.

[10] S. Adachi, Review—Photoluminescence properties of Cr^{3+}-activated fluoride phosphors, ECS J. Solid State Sci. Technol. 10 (3) (2021) 036001.

[11] S. He, L. Zhang, H. Wu, H. Wu, G. Pan, Z. Hao, X. Zhang, L. Zhang, H. Zhang, J. Zhang, Broadband near-infrared (NIR) emission realized by the crystal-field engineering of $Y_{3-x}Ca_xAl_{5-x}Si_xO_{12}$:$Cr^{3+}$ (x = 0–2.0) garnet phosphors, J. Mater. Chem. C 8 (2020) 1981–1988.

[12] V. Rajendran, M.-H. Fang, G.N.D. Guzman, T. Lesniewski, S. Mahlik, M. Grinberg, G. Leniec, S.M. Kaczmarek, Y.-S. Lin, K.-M. Lu, C.-M. Lin, H.o. Chang, S.-F. Hu, R.-S. Liu, Super broadband near-infrared phosphors with high radiant flux as future light sources for spectroscopy applications, ACS Energy Lett. 3 (11) (2018) 2679–2684.

[13] J.A. Lai, W.H. Shen, J.B. Qiu, D.C. Zhou, Z.W. Long, Y. Yang, K. Zhang, I. Khan, Q. Wang, Broadband near-infrared emission enhancement in $K_2Ga_2Sn_6O_{16}$:Cr^{3+} phosphor by electron-lattice coupling regulation, J. Am. Ceram. Soc. 103 (2020) 5067–5075.

[14] G.C. Liu, T. Hu, M.S. Molokeev, Z.G. Xia, Li/Na substitution and Yb^{3+} co-doping enabling tunable near-infrared emission in $LiIn_2SbO_6$:Cr^{3+} phosphors for light-emitting diode, iScience 24 (2021), 102250.

[15] F.Y. Zhao, Z. Song, J. Zhao, Q.L. Liu, Double perovskite $Cs_2AgInCl_6$:Cr^{3+}: broadband and near-infrared luminescent materials, Inorg, Chem. Front. 6 (2019) 3621–3628.

[16] W.T. Huang, C.L. Cheng, Z. Bao, C.W. Yang, K.M. Lu, C.Y. Kang, C.M. Lin, R.S. Liu, Broadband Cr^{3+}, Sn^{4+}-doped oxide nanophosphors for infrared mini light-emitting diodes, Angew. Chem. Int. Edit. 58 (2019) 2069–2072.

[17] M.-H. Fang, K.-C. Chen, N. Majewska, T. Leśniewski, S. Mahlik, G. Leniec, S. M. Kaczmarek, C.-W. Yang, K.-M. Lu, H.-S. Sheu, R.-S. Liu, Hidden structural evolution and bond valence control in near-infrared phosphors for light-emitting diodes, ACS Energy Lett. 6 (1) (2021) 109–114.

[18] D.C. Huang, H.M. Zhu, Z.H. Deng, H.Y. Yang, J. Hu, S.S. Liang, D.J. Chen, E. Ma, W. Guo, A highly efficient and thermally stable broadband Cr^{3+}-activated double borate phosphor for near-infrared light-emitting diodes, J. Mater. Chem. C 9 (2021) 164–172.

[19] M.-H. Fang, G.N.A. De Guzman, Z. Bao, N. Majewska, S. Mahlik, M. Grinberg, G. Leniec, S.M. Kaczmarek, C.-W. Yang, K.-M. Lu, H.-S. Sheu, S.-F. Hu, R.-S. Liu, Ultra-high-efficiency near-infrared Ga_2O_3:Cr^{3+} phosphor and controlling of phytochrome, J. Mater. Chem. C 8 (32) (2020) 11013–11017.

[20] G. Zheng, W. Xiao, H. Wu, J. Wu, X. Liu, J. Qiu, Near-Unity and Zero-thermal-quenching far-red-emitting composite ceramics via pressureless glass crystallization, Laser Photonics Rev. 15 (7) (2021) 2100060.

[21] A. Zabiliūtè, S. Butkutè, A. Žukauskas, P. Vitta, A. Kareiva, Sol-gel synthesized far-red chromium-doped garnet phosphors for phosphor-conversion light-emitting diodes that meet the photomorphogenetic needs of plants, Appl. Optics 53 (5) (2014) 907–914.

[22] D.J. Liu, G.G. Li, P.P. Dang, Q.Q. Zhang, Y. Wei, H.Z. Lian, M.M. Shang, C.C. Lin, J. Lin, Simultaneous broadening and enhancement of Cr^{3+} photoluminescence in $LiIn_2SbO_6$ by chemical unit cosubstitution: night-vision and near-infrared

spectroscopy detection applications, Angew. Chem. Int. Edit. 60 (2021) 14644–14649.

[23] E.T. Basore, W. Xiao, X. Liu, J. Wu, J. Qiu, Broadband near-infrared garnet phosphors with near-unity internal quantum efficiency, Adv. Opt. Mater. 8 (12) (2020) 2000296.

[24] J.K. Li, J.G. Li, Z.J. Zhang, X.L. Wu, S.H. Liu, X.D. Li, X.D. Sun, Y.S. Sakka, Gadolinium aluminate garnet ($Gd_3Al_5O_{12}$): crystal structure stabilization via lutetium doping and properties of the ($Gd_{1-x}Lu_x)_3Al_5O_{12}$ solid solutions (x = 0–0.5), J. Am. Ceram. Soc. 95 (3) (2012) 931–936.

[25] L.Q. Yao, Q.Y. Shao, X.X. Xu, Y. Dong, C. Liang, J.H. He, J.Q. Jiang, Broadband emission of single-phase $Ca_3Sc_2Si_3O_{12}:Cr^{3+}/Ln^{3+}$ (Ln = Nd, Yb, Ce) phosphors for novel solid-state light sources with visible to near-infrared light output, Ceram. Int. 45 (11) (2019) 14249–14255.

[26] Z.W. Jia, C.X. Yuan, Y.F. Liu, X.J. Wang, P. Sun, L. Wang, H.C. Jiang, J. Jiang, Strategies to approach high performance in Cr^{3+}-doped phosphors for high-power NIR-LED light sources, Light: Sci, Appl. 9 (2020) 86.

[27] H. Sawada, Electron density study of garnets: $Z_3Ga_5O_{12}$: Z= Nd, Sm, Gd, Tb, J. Solid State Chem. 132 (2) (1997) 300–307.

[28] V. Singh, R.V.S.S.N. Ravikumar, G. Sivaramaiah, J.L. Rao, S.H. Kim, Investigations of the optical and EPR properties of $LiGa_5O_8:Cr^{3+}$ phosphor, Mater. Res. Bull. 61 (2015) 183–188.

[29] I.-W. Kim, S. Kaur, A. Yadav, A.S. Rao, S. Saravanakumar, J.L. Rao, V. Singh, Structural, luminescence and EPR properties of deep red emitting $MgY_2Al_4SiO_{12}$: Cr^{3+} garnet phosphor, J. Lumin. 220 (2020) 116975.

[30] A. Edgar, D.R. Hutton, Exchange-coupled pairs of Cr^{3+} ions in emerald, J. Phys. C: Solid State Phys. 11 (1978) 5051–5063.

[31] J.A. Lai, J.H. Zhou, Z.W. Long, J.B. Qiu, D.C. Zhou, Y. Yang, K. Zhang, W.H. Shen, Q. Wang, Broadband near-infrared emitting from $Li_{1.6}Zn_{1.6}Sn_{2.8}O_8:Cr^{3+}$ phosphor by two-site occupation and Al^{3+} cationic regulation, Mater. Des. 192 (2020), 108701.

[32] G.C. Liu, M.S. Molokeev, B.F. Lei, Z.G. Xia, Two-site Cr^{3+} occupation in $MgTa_2O_6$: Cr^{3+} phosphor toward broadband near-infrared emission for vessel visualization, J. Mater. Chem. C 8 (2020) 9322–9328.

[33] Y. Tanabe, S. Sugano, On the Absorption Spectra of Complex Ions II, J. Phys. Soc. Jpn. 9 (1954) 766–779.

[34] S. Adachi, New analysis model for the determination of Racah and crystal-field splitting parameters: Verification and case studies, ECS J. Solid State Sci. Technol. 9 (4) (2020) 046004.

[35] X.X. Xu, Q.Y. Shao, L.Q. Yao, Y. Dong, J.Q. Jiang, Highly efficient and thermally stable Cr^{3+}-activated silicate phosphors for broadband near-infrared LED applications, Chem. Eng. J. 383 (2020), 123108.

[36] H. Zeng, T. Zhou, L. Wang, R.-J. Xie, Two-site occupation for exploring ultra-broadband near-infrared phosphor double-perovskite $La_2MgZrO_6:Cr^{3+}$, Chem. Mater. 31 (14) (2019) 5245–5253.

[37] Q.Y. Shao, H. Ding, L.Q. Yao, J.F. Xu, C. Liang, J.Q. Jiang, Photoluminescence properties of a $ScBO_3:Cr^{3+}$ phosphor and its applications for broadband near-infrared LEDs, RSC Adv. 8 (2018) 12035–12042.

[38] S.Q. Liu, Z.Z. Wang, H. Cai, Z. Song, Q.L. Liu, Highly efficient near-infrared phosphor $LaMgGa_{11}O_{19}:Cr^{3+}$, Inorg. Chem. Front. 7 (6) (2020) 1467–1473.

[39] B. Malysa, A. Meijerink, T. Jüstel, Temperature dependent Cr^{3+} photoluminescence in garnets of the type $X_3Sc_2Ga_3O_{12}$ (X = Lu, Y, Gd, La), J. Lumin. 202 (2018) 523–531.

[40] M.G. Brik, N.M. Avrama, Crystal field analysis and electron-phonon coupling in $Sc_2O_3:Cr^{3+}$, Z. Naturforsch. a 59 (2004) 799–803.

[41] G.A. Torchiaa, O. Martinez-Matosb, N.M. Khaidukovc, J.O. Tocho, Phonon coupling of Cr^{3+} ions in Cs_2NaAlF_6 crystals, Solid State Commun. 130 (2004) 159–163.

[42] B. Malysa, A. Meijerink, T. Jüstel, Temperature dependent luminescence Cr^{3+}-doped $GdAl_3(BO_3)_4$ and $YAl_3(BO_3)_4$, J. Lumin. 171 (2016) 246–253.

[43] E.H. Song, H. Ming, Y.Y. Zhou, F.Q. He, J.C. Wu, Z.G. Xia, Q.Y. Zhang, Cr^{3+}-doped Sc-based fluoride enabling highly efficient near infrared luminescence: a case study of $K_2NaScF_6:Cr^{3+}$, Laser Photonics Rev. 15 (2) (2021) 2000410.

[44] L. Yao, Q. Shao, S. Han, C. Liang, J. He, J. Jiang, Enhancing near-infrared photoluminescence intensity and spectral properties in Yb^{3+} Codoped $LiScP_2O_7:Cr^{3+}$, Chem. Mater. 32 (6) (2020) 2430–2439.

[45] S. He, L.L. Zhang, H. Wu, H.J. Wu, G.H. Pan, Z.D. Hao, X. Zhang, L.G. Zhang, H. Zhang, J.H. Zhang, Efficient super broadband NIR $Ca_2LuZr_2Al_3O_{12}:Cr^{3+}$, Yb^{3+} garnet phosphor for pc-LED light source toward NIR spectroscopy applications, Adv. Opt. Mater. 8 (6) (2020) 1901684.

[46] J. Shin, K. Kim, H. Kang, I.S. Zulfugarov, G. Bae, C.-H. Lee, D. Lee, G. Choi, Phytochromes promote seedling light responses by inhibiting four negatively-acting phytochrome-interacting factors, Proc. Natl. Acad. Sci. U. S. A. 106 (18) (2009) 7660–7665.